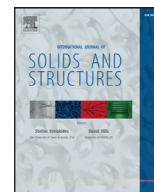




Contents lists available at ScienceDirect

## International Journal of Solids and Structures

journal homepage: [www.elsevier.com/locate/ijssolstr](http://www.elsevier.com/locate/ijssolstr)

# Effect of anisotropy and differential work hardening on the failure prediction of AZ31B magnesium sheet at room temperature

Kanghwan Ahn\*, Min-Hong Seo

Materials Forming Research Group, POSCO Global R&amp;D Center 100, Songdogwahak-ro, Yeonsu-gu, Incheon 406-840, Republic of Korea

## ARTICLE INFO

## Article history:

Received 9 May 2017

Revised 27 August 2017

Available online xxx

## Keywords:

AZ31B Mg sheet

Maximum shear stress criterion

Non-associated flow rule

Failure limit

Differential work hardening

## ABSTRACT

In order to predict the failure of AZ31B Mg sheet at room temperature under uniaxial and biaxial loading paths, analytical expressions based on the maximum shear stress criterion in conjunction with the quadratic anisotropic yield function and plastic potential were developed. By utilizing the formulations based on the associated flow rule (AFR) and the non-associated flow rule (NAFR), different levels of material anisotropy were considered with the developed equations. Material coefficients of anisotropy were obtained from tensile and bulge tests taking into account the differential work hardening of AZ31B Mg sheet. Failure predictions were performed and compared with the experimental failure strains measured by the hemispherical dome tests at room temperature. In the failure prediction of AZ31B Mg sheet, it was found that the material anisotropy and the differential work hardening exhibited by the AZ31B Mg sheet were primary factors which have a major influence on the results of failure prediction, and the formulations based on the NAFR with the material coefficients obtained by taking into account the differential work hardening showed good accuracy by yielding failure predictions close to the experimentally measured failure strains.

© 2018 Elsevier Ltd. All rights reserved.

## 1. Introduction

Magnesium alloys have been widely used for industrial applications for which weight reduction is highly required. Although a variety of wrought magnesium alloys have been developed to date, most magnesium alloys commercially used in industries are still in the form of castings. The inferior formability of wrought magnesium alloys at room temperature resulting from their HCP (Hexagonal Close Packed) crystal structure (Shackelford, 2009) is a primary reason why their usage is not widespread in commercial applications. For this reason, there have been continuous efforts to enhance the formability of wrought magnesium alloys (Huang et al., 2009; Bohlen et al., 2007; Suh et al., 2014), and thereby to extend their commercial applications.

The magnesium alloy AZ31B is a typical wrought magnesium alloy primarily used for manufacturing rolled sheet products. The AZ31B Mg rolled sheet has a strength comparable to that of the mild steel sheet (Kim et al., 2008), but has a limited formability at room temperature, so that any stamping process is normally conducted at elevated temperatures higher than 200 °C (Doege and Droder, 2001). For this reason, forming limits are mostly measured at elevated temperatures. In some cases, such as the formabil-

ity evaluation of parts with a simple geometry formable at room temperature or performance evaluations like crashworthiness, the forming limit (or failure limit) curve at room temperature is essentially required to make such evaluations.

The AZ31B Mg sheet has a brittle nature at room temperature, showing little necking before failure occurs (Agnew and Duygulu, 2005; Lou et al., 2007). Therefore, to predict a failure limit of AZ31B Mg sheet, it would be more reasonable to use a failure model suitable for its brittleness rather than using common ductile failure models based on the theory of localized necking (e.g. Hill's bifurcation theory; Hill, 1952 or the M-K model; Marciniak and Kuczynski, 1967) found in the field of sheet metal forming. Among numerous research works on the failure prediction of sheet metals found in the literature, Wierzbicki et al. (2005) summarized the performances of seven practical fracture criteria under the plane stress condition, while conducting comparative studies with these criteria in relation to experimental data. In their work, it was found that the maximum shear stress criterion, which is not based on the necking theory, followed the experimental fracture points well despite its small number of material parameters in comparison to the other failure criteria. Li et al. (2010) showed that the modified Mohr–Coulomb fracture criterion, which is in effect equivalent to the maximum shear stress criterion in the space of positive in-plane principal stresses, well captured the shear-induced fractures of advanced high strength steels. Although a variety of

\* Corresponding author.

E-mail address: [akhwan21@posco.com](mailto:akhwan21@posco.com) (K. Ahn).

failure models were explored by these authors, material anisotropy was not considered in their models. Failure predictions considering material anisotropy were made by Lin et al. (2010) with the maximum shear stress criterion. In their work, the anisotropic yield functions Hill 1948 and Yld2000-2d were incorporated into numerical programming to predict the forming limits of steel and aluminum sheets, making an attempt to predict the localized necking by means of the maximum shear stress criterion. Meanwhile, there were other approaches to predict the failure of Mg sheets by employing viscoplastic crystal plasticity models at room and elevated temperatures (Neil and Agnew, 2009; Wang et al., 2011, 2015). In all those works, estimations of failure were made by utilizing the M-K model, a failure model for ductile metals, even at room temperature.

In this work, the anisotropic properties of AZ31B Mg sheet associated with its failure behavior were considered by using the plane stress version of the quadratic anisotropic yield function proposed by Hill (1948), i.e., Hill 1948 yield function. Due to its simplicity and the minimal number of material parameters, Hill 1948 yield function is suitable for deriving analytical expressions for many plasticity problems. However, since it has only four parameters of anisotropy under the plane stress condition, it is not possible to account for completely all of the three yield stresses and three  $R$ -values (width to thickness strain ratios) measured along the  $0^\circ$ ,  $45^\circ$  and  $90^\circ$  to the rolling direction (Chung et al., 2011). An alternative way to resolve this limitation without resorting to a higher order yield function is to introduce the NAFR, i.e., not using the same function for the yield function and the plastic potential. Stoughton (2002) discussed the validity of the NAFR in sheet metal forming and showed that the yield function and the plastic potential differently defined by the quadratic anisotropic function well represented the anisotropic material data measured at evenly divided angles between the rolling and the transverse directions. Park and Chung (2012) employed the NAFR to predict the earing profiles in circular cup drawing, while utilizing the quadratic anisotropic functions for the yield function and the plastic potential, respectively.

Analytical expressions to make failure predictions of the AZ31B Mg sheet between uniaxial and balanced biaxial loading paths were derived in this work based on the maximum shear stress criterion in conjunction with the quadratic anisotropic yield function and the plastic potential within the framework of the AFR and the NAFR. Material coefficients of the failure prediction equation were determined by tensile and bulge tests, while the failure strains of AZ31B Mg sheet were measured by the hemispherical dome tests. The effects of material anisotropy on failure prediction were explored with the failure prediction equations by imposing further restrictions on their material coefficients of anisotropy, and the differences made by using the AFR and the NAFR in formulations were explored as well. The procedure to determine the material coefficients of anisotropy considering the differential work hardening of AZ31B Mg sheet was addressed with the influence of those coefficients on failure predictions.

## 2. Formulation

### 2.1. Maximum shear stress criterion

For the material subjected to the increasing external load, the maximum shear stress criterion defines material failure as the maximum internal shear stress of the material reaches a critical value. For the planar sheet material whose thickness is relatively small compared to the other material dimensions, the plane stress condition is usually assumed, and with a further assumption that the directions of principal stresses are coincident with those of the symmetry axes of the orthotropic sheet material, the internal

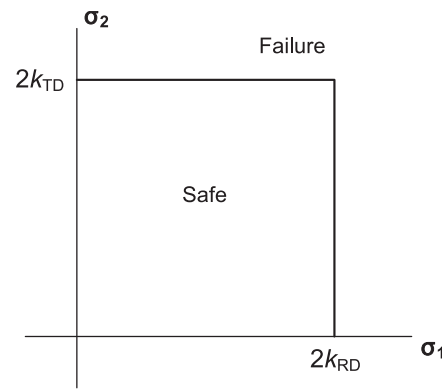


Fig. 1. Failure condition of the maximum shear stress criterion in the in-plane principal stress space.

stress state can be defined by the two principal stress components,  $\sigma_1$  and  $\sigma_2$ , where 1 and 2 denote stress components parallel and perpendicular to the direction of rolling. Under loading conditions where both in-plane principal stresses are positive (i.e., principal stresses are either in a state of  $\sigma_1 \geq \sigma_2 \geq 0$  or  $\sigma_2 \geq \sigma_1 \geq 0$ ), the maximum shear stress in the sheet material is no longer present within the 1–2 plane (except for the condition where the minor in-plane principal stress is equal to zero.). This is because  $\sigma_3$ , a third principal stress component whose direction is normal to the 1–2 plane, is considered to be zero under the plane stress condition. Therefore, under loading conditions that both in-plane principal stresses are positive and proportional to each other, failure of anisotropic sheet materials occurs, according to the maximum shear stress criterion, as the increasing principal stresses first reach one of the following conditions:

$$\frac{\sigma_1}{2} = k_{RD}, \quad \frac{\sigma_2}{2} = k_{TD} \quad (1)$$

where  $k_{RD}$  and  $k_{TD}$  are the critical shear stresses of failure along the rolling and transverse directions, respectively. In Fig. 1, the failure condition corresponding to Eq. (1) is illustrated in the first quadrant of the in-plane principal stress space, which covers stress states ranging from the uniaxial to balanced biaxial loading conditions.

It should be noted that in this work, all the formulations and tests are made under the conditions that the directions of principal stresses coincide with the axes of material symmetry, while the transverse direction of anisotropic rolled sheet is chosen to be the reference direction of material as well as the direction of major loading, i.e., the condition  $\sigma_2 \geq \sigma_1 \geq 0$  holds throughout this work.

### 2.2. Yield criterion and plastic potential

Under the plane stress condition with an assumption that the directions of principal stresses coincide with the symmetry axes of an orthotropic sheet material, the quadratic anisotropic yield criterion proposed by Hill (1948) can be defined in the principal stress space as

$$(G + H)\sigma_1^2 - 2H\sigma_1\sigma_2 + (H + F)\sigma_2^2 - 1 = 0, \quad (2)$$

where  $F$ ,  $G$  and  $H$  are the coefficients of material anisotropy. To more precisely account for the yield stress for any loading condition, three coefficients of anisotropy in Eq. (2) were determined by using three yield stresses, rather than by using three  $R$ -values,

according to the following relationships:

$$2G = \frac{1}{X^2} + \frac{1}{B^2} - \frac{1}{Y^2}, \quad 2F = \frac{1}{Y^2} + \frac{1}{B^2} - \frac{1}{X^2} \quad \text{and} \quad 2H = \frac{1}{X^2} + \frac{1}{Y^2} - \frac{1}{B^2}, \quad (3)$$

where the coefficients  $X$  and  $Y$  represent the yield stresses along the rolling and transverse directions, respectively, while the coefficient  $B$  represents the balanced biaxial yield stress. Substituting Eq. (3) into Eq. (2) with the assumption of isotropic hardening, it follows that

$$\bar{\sigma} = \sqrt{\frac{Y^2}{X^2} \sigma_1^2 - \left(1 + \frac{Y^2}{X^2} - \frac{Y^2}{B^2}\right) \sigma_1 \sigma_2 + \sigma_2^2} = Y(\bar{\varepsilon}), \quad (4)$$

where  $\bar{\sigma}$  denotes the effective stress, and  $Y(\bar{\varepsilon})$  denotes the yield stress along the transverse direction as a function of the effective strain  $\bar{\varepsilon}$ .  $Y(\bar{\varepsilon})$  determines the magnitude of the effective stress. Note that the effective stress in Eq. (4) was defined by choosing the transverse direction as its reference direction.

The plastic potential, whose gradient defines the direction of the plastic strain increment, was obtained from Eq. (2), the same equation defining the yield condition, but with different coefficients of anisotropy determined by three measurements: a yield stress along the transverse direction and two  $R$ -values along the rolling and transverse directions. The plastic potential  $\Phi$  defined in this manner is given by

$$\Phi = \sqrt{\frac{1+R_0}{R_0} \sigma_1^2 - 2\sigma_1 \sigma_2 + \frac{1+R_{90}}{R_{90}} \sigma_2^2}, \quad (5)$$

where  $R_0$  and  $R_{90}$  denote  $R$ -values measured along the rolling and transverse directions, respectively.

### 2.3. Non-associated flow rule

Under the framework of the NAFR, the plastic potential function is defined independently of the yield function. The plastic strain increment is obtained from the gradient of the plastic potential by the following relationship:

$$d\varepsilon_i^p = d\lambda \frac{\partial \Phi}{\partial \sigma_i}, \quad (6)$$

where  $d\lambda$  is the plastic multiplier to define the magnitude of the plastic strain increment. Note that if the directions of principal stress coincide with the symmetry axes of an orthotropic sheet material, then the principal directions of stress and plastic strain increment are coincident. Substituting the plastic potential defined in Eq. (5) into Eq. (6),  $d\lambda$  can be represented as a function of the principal plastic strain increment as follows:

$$d\lambda = \sqrt{\frac{R_0 R_{90}}{1+R_0+R_{90}}} \left\{ \frac{1+R_{90}}{R_{90}} (d\varepsilon_1^p)^2 + 2d\varepsilon_1^p d\varepsilon_2^p + \frac{1+R_0}{R_0} (d\varepsilon_2^p)^2 \right\}. \quad (7)$$

Eq. (7) can be further modified into the following form by considering Eqs. (5) and (6):

$$d\lambda = \frac{\sqrt{K_0 \beta^2 - 2\beta + K_{90}}}{K_{90} - \beta} d\varepsilon_2^p, \quad (8)$$

where

$$K_0 = \frac{1+R_0}{R_0}, \quad K_{90} = \frac{1+R_{90}}{R_{90}} \quad \text{and} \quad \beta = \frac{\sigma_1}{\sigma_2} \quad (9)$$

Here, the stress ratio  $\beta$  has a range varying from 0 (i.e., uniaxial loading) to 1 (i.e., balanced biaxial loading). Considering the plastic

work equivalence principle with the NAFR defined in Eq. (6), the following relationships are obtained:

$$dW^p = \bar{\sigma} d\bar{\varepsilon}^p = \sigma_i d\varepsilon_i^p = \sigma_i d\lambda \frac{\partial \Phi}{\partial \sigma_i} = d\lambda \Phi, \quad (10)$$

where the intrinsic property of the function  $\Phi$ , homogeneous of order 1, was utilized. Then, from Eq. (10), the effective plastic strain increment is defined as

$$d\bar{\varepsilon}^p = \frac{\Phi}{\bar{\sigma}} d\lambda. \quad (11)$$

### 2.4. Equations of failure prediction

Under the proportional loading condition, plastic strain increments given by Eq. (6) also have a proportional relationship considering Eqs. (5) and (6). Therefore, integrating Eq. (10) and substituting Eqs. (4), (5) and (8) into Eq. (10) gives

$$\bar{\varepsilon}^p = \frac{\Phi}{\bar{\sigma}} \lambda = G(\beta) \varepsilon_2^p, \quad (12)$$

where

$$G(\beta) = \frac{K_0 \beta^2 - 2\beta + K_{90}}{\sqrt{\frac{Y^2}{X^2} \beta^2 - \left(1 + \frac{Y^2}{X^2} - \frac{Y^2}{B^2}\right) \beta + 1} (K_{90} - \beta)}. \quad (13)$$

The material hardening of AZ31B Mg sheet is represented by using the Swift equation as

$$\bar{\sigma} = Y(\bar{\varepsilon}) = K(\bar{\varepsilon}^p + \bar{\varepsilon}_0^p)^n, \quad (14)$$

where  $K$ ,  $\bar{\varepsilon}_0^p$  and  $n$  are the coefficients of material hardening to be determined by applying the least square fitting to the uniaxial stress-strain curve measured along the transverse direction. Note that in this analysis, it is supposed that the transverse direction is the direction of major principal stress. Let  $\sigma_f$  be the major principal stress at failure measured along the transverse direction, then the critical shear stress of failure can be obtained from Eq. (1) by the following form:

$$k_{TD} = \frac{\sigma_f}{2}. \quad (15)$$

As the maximum shear stress in the sheet material reaches the critical value given in Eq. (15), the corresponding effective stress can be found by considering Eqs. (1) and (4) and has a form

$$\bar{\sigma}_f = 2k_{TD} \sqrt{\frac{Y^2}{X^2} \beta^2 - \left(1 + \frac{Y^2}{X^2} - \frac{Y^2}{B^2}\right) \beta + 1}, \quad (16)$$

where  $\bar{\sigma}_f$  denotes the effective stress at failure. Substituting Eq. (16) into Eq. (14) with further manipulations, the effective plastic strain at failure is obtained as

$$\bar{\varepsilon}_f^p = \left( \frac{Y^2}{X^2} \beta^2 - \left(1 + \frac{Y^2}{X^2} - \frac{Y^2}{B^2}\right) \beta + 1 \right)^{\frac{1}{2n}} \left( \frac{2k_{TD}}{K} \right)^{\frac{1}{n}} - \bar{\varepsilon}_0^p, \quad (17)$$

where  $\bar{\varepsilon}_f^p$  denotes the effective plastic strain at failure. Considering Eq. (17) further with Eqs. (6) and (12), the principal plastic strains at failure are finally obtained as

$$(\varepsilon_2^p)_f = \frac{\left( \frac{Y^2}{X^2} \beta^2 - \left(1 + \frac{Y^2}{X^2} - \frac{Y^2}{B^2}\right) \beta + 1 \right)^{\frac{1}{2n}} \left( \frac{2k_{TD}}{K} \right)^{\frac{1}{n}} - \bar{\varepsilon}_0^p}{G(\beta)} \quad \text{and} \quad (\varepsilon_1^p)_f = \frac{K_0 \beta - 1}{K_{90} - \beta} (\varepsilon_2^p)_f \quad \text{for} \quad 0 \leq \beta \leq 1, \quad (18)$$

where  $(\varepsilon_1^p)_f$  and  $(\varepsilon_2^p)_f$  denote the principal plastic strain components at which failure occurs. The failure plastic strains in Eq. (18) depend on the stress ratio  $\beta$  (or equivalently deformation paths). Note that the expressions in Eq. (18) are valid under the proportional loading condition.

Imposing the condition of normal anisotropy (i.e.,  $X=Y$  and  $R_0 = R_{90} = \bar{R} = (R_0 + R_{90})/2$ ) on Eq. (18) leads to the following forms:

$$(\varepsilon_2^p)_f = \frac{(\beta^2 - (2 - \frac{\gamma^2}{\beta^2})\beta + 1)^{\frac{1}{2n}} (\frac{2k_{TD}}{K})^{\frac{1}{n}} - \bar{\varepsilon}_0^p}{\bar{G}(\beta)} \text{ and}$$

$$(\varepsilon_1^p)_f = \frac{\bar{K}\beta - 1}{\bar{K} - \beta} (\varepsilon_2^p)_f \text{ for } 0 \leq \beta \leq 1, \quad (19)$$

where

$$\bar{G}(\beta) = \frac{\bar{K}\beta^2 - 2\beta + \bar{K}}{\sqrt{\beta^2 - (2 - \frac{\gamma^2}{\beta^2})\beta + 1} (\bar{K} - \beta)} \text{ and } \bar{K} = \frac{1 + \bar{R}}{\bar{R}}. \quad (20)$$

For comparison purposes, the AFR was also employed here to derive the expression for failure. Since it is common practice to take  $R$ -values to represent the anisotropy of the quadratic anisotropic yield function, the onset condition of yielding was defined by the following yield criterion:

$$F = \bar{\sigma}_A - Y(\bar{\varepsilon}) = 0, \quad (21)$$

where the effective stress  $\bar{\sigma}_A$  for the AFR is defined as

$$\bar{\sigma}_A = \sqrt{\frac{R_{90}}{1 + R_{90}}} \sqrt{\frac{1 + R_0}{R_0} \sigma_1^2 - 2\sigma_1\sigma_2 + \frac{1 + R_{90}}{R_{90}} \sigma_2^2}. \quad (22)$$

Here, the effective stress  $\bar{\sigma}_A$  and the plastic potential  $\Phi$  of the NAFR defined in Eq. (5) are functions of the same kind, but only differ by an additional multiplication constant  $\sqrt{R_{90}/(1 + R_{90})}$  in Eq. (22), which was introduced to adjust the magnitude of the effective stress to the yield stress measured along the transverse direction. Following the same procedure that leads to the failure condition in Eq. (18) with the effective stress  $\bar{\sigma}_A$  instead of the effective stress  $\bar{\sigma}$  and the plastic potential  $\Phi$ , the failure condition within the framework of the AFR is given by

$$(\varepsilon_2^p)_f = \frac{(\frac{K_0}{K_{90}}\beta^2 - \frac{2\beta}{K_{90}} + 1)^{\frac{1}{2n}} (\frac{2k_{TD}}{K})^{\frac{1}{n}} - \bar{\varepsilon}_0^p}{\sqrt{K_{90}}\sqrt{K_0\beta^2 - 2\beta + K_{90}}} (K_{90} - \beta) \text{ and}$$

$$(\varepsilon_1^p)_f = \frac{K_0\beta - 1}{K_{90} - \beta} (\varepsilon_2^p)_f \text{ for } 0 \leq \beta \leq 1. \quad (23)$$

By imposing further restrictions on Eqs. (19) and (20) with the condition that  $Y=B$  and  $\bar{R} = 1$ , or on Eq. (23) with the condition of  $K_0 = K_{90} = 2$ , both of these equations identically reduce to the failure condition of the isotropic material, i.e.,

$$(\varepsilon_2^p)_f = \frac{(\beta^2 - \beta + 1)^{\frac{1}{2n}} (\frac{2k}{K})^{\frac{1}{n}} - \bar{\varepsilon}_0^p}{2\sqrt{\beta^2 - \beta + 1}} (2 - \beta) \text{ and}$$

$$(\varepsilon_1^p)_f = \frac{2\beta - 1}{2 - \beta} (\varepsilon_2^p)_f \text{ for } 0 \leq \beta \leq 1, \quad (24)$$

where,  $k = k_{RD} = k_{TD}$ .

### 3. Material characterization

#### 3.1. Uniaxial tensile test

To characterize the mechanical properties and the hardening behavior of the Mg sheet, uniaxial tensile tests were conducted. The Mg sheet investigated in this work is an annealed sheet made of AZ31B (3 wt% Al, 1 wt% Zn) alloy, and has a thickness of 1.2 mm. Tensile test specimens were made by machining according to the dimensions specified in the test standard ASTM E8M. Specimens were prepared for the rolling and transverse directions respectively to characterize the anisotropic mechanical properties. Tensile tests were carried out using the universal testing machine with a

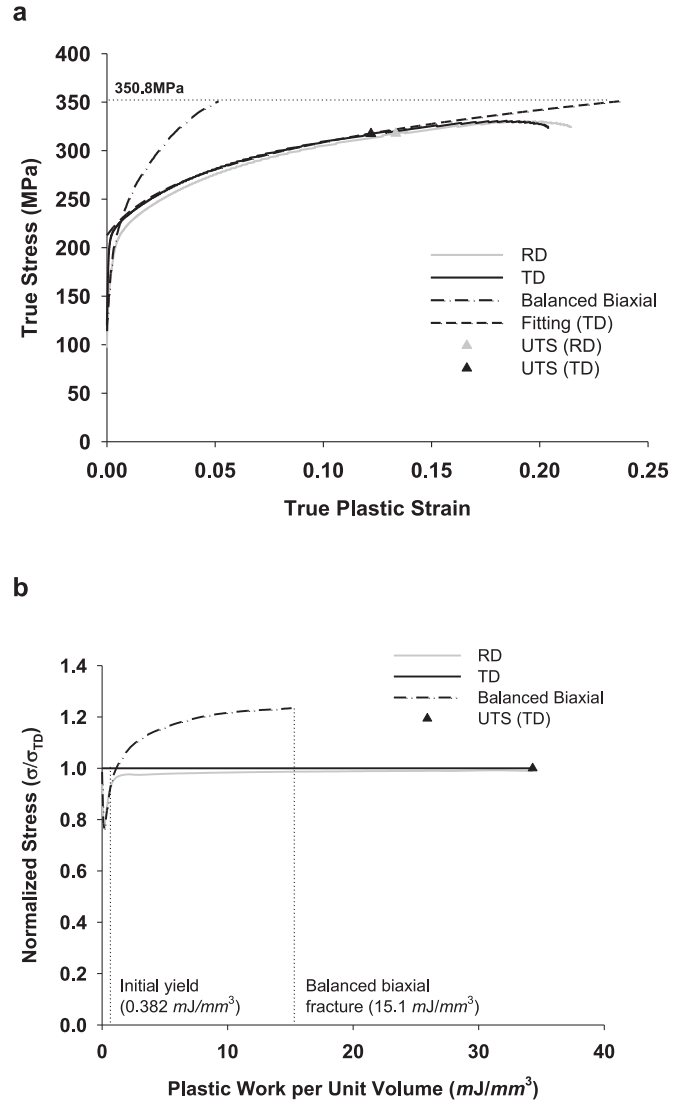


Fig. 2. Hardening curves of AZ31B Mg sheet (a) measured along the rolling and transverse directions as well as under the balanced biaxial loading condition and (b) normalized by the plastic work equivalent stresses along the transverse direction with the horizontal axis shown in terms of the plastic work per unit volume.

crosshead speed of 3 mm/min to produce the nominal strain rate of 0.001/s.

The measured mechanical properties were listed in Table 1, in which initial yield strengths (YS), ultimate tensile strengths (UTS), uniform elongations ( $\varepsilon_{UTS}$ ),  $R$ -values and total elongations (TE) were summarized. The  $R$ -values were measured automatically for the strain range of 5–10% by following the procedure specified in the standard ISO 10113:2006(E), while the elastic modulus ( $E$ ) and the Poisson's ratio ( $\nu$ ) were obtained from literature (Cubberly et al., 1979). The initial yield strength (or initial yield stress) along the transverse direction was determined by 0.2% offset method, and the corresponding plastic work up to this yield point was used as a reference value to determine the plastic work equivalent yield stress along the rolling direction. The measured uniaxial hardening curves were shown in Fig. 2(a), in which the hardening curve along the transverse direction was shown along with its least square fitting curve. To fit the curve, the Swift equation in Eq. (14) was used for the interval ranging from the 0.2% offset yield stress to the ultimate tensile strength of the hardening curve. Note that the horizontal axis in Fig. 2(a) denotes the true



**Table 1**  
Mechanical properties of the AZ31B Mg sheet.

Loading condition	$E^a$ (GPa)	$\nu^a$	YS (MPa)	UTS (MPa)	$\varepsilon_{UTS}$ (%)	TE (%)	R	Plastic work equivalent stress (MPa)
Simple tension (RD)	45.0	0.35	182.8	278.5	14.7	23.6	2.2	283.7
Simple tension (TD)			212.4	280.2	13.9	22.1	2.9	287.4
Balanced biaxial			184.2	–	–	5.3	–	350.8 <sup>b</sup>

<sup>a</sup> Referred by Cubberly et al. (1979).

<sup>b</sup> Failure stress of the balanced biaxial flow curve.

**Table 2**  
Coefficients of the Swift equation and failure prediction equations of the AZ31B Mg sheet.

$K$	$\bar{\varepsilon}_0^p$	$n$	$k_{TD}$	$K_0$	$K_{90}$	$\bar{K}$	$X$	$Y$	$B$	$X'$	$Y'$	$B'$
438.3	0.0107	0.16	175.4	1.45	1.35	1.39	271.0	275.8	331.9	239.4	248.7	274.5

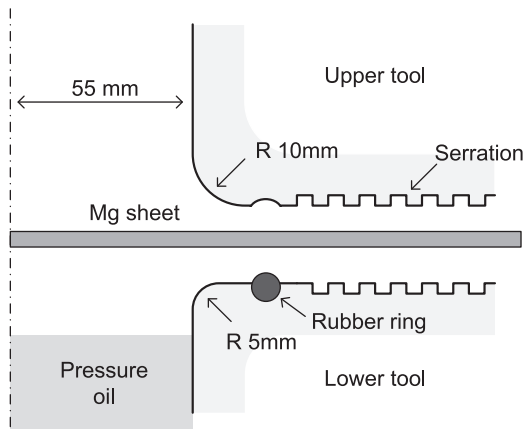


**Fig. 3.** Schematic view of axisymmetric tools of the hydraulic bulge tester with their dimensions.

plastic strain, which implies that the hardening curves in Fig. 2(a) were plotted after removing elastic strains from the measured hardening curve. The resulting coefficients of the fitting equation (i.e.,  $K$ ,  $\bar{\varepsilon}_0^p$  and  $n$ ) are summarized in Table 2.

In Fig. 2(a), a point corresponding to the ultimate tensile strength was designated on the hardening curve measured for each direction, which indicates the occurrence of diffuse neck in the uniaxial tensile tests of the AZ31B Mg sheet. Consequently, the remaining hardening curve after this point cannot be considered as the true material hardening curve. The hardening behavior after the ultimate tensile strength, therefore, was estimated by extrapolation utilizing the Swift equation. Concerning the material anisotropic properties summarized in Table 1, it is found that the AZ31B Mg sheet has a rather large  $R$ -value along each direction. This could be attributed to the limited slip systems at room temperature and the strong texture orientation of AZ31B Mg sheets (Lou et al., 2007).

### 3.2. Hydraulic bulge test

To measure the hardening curve under the balanced biaxial loading condition, bulge tests were conducted using a hydraulic bulge tester having a circular opening in the die. The axisymmetric tool geometry and its dimensions were illustrated in Fig. 3. The circular hole in the tool has a diameter of 110 mm, while the upper tool has a rather large corner radius of 10 mm to prevent failures of specimens at this tool corner, and serrations were formed on each surface of the upper and lower tools to hold specimens firmly, instead of using a lock bead that might cause cracks in specimens by making severe deformation. To prevent a leakage of pressure oil, a

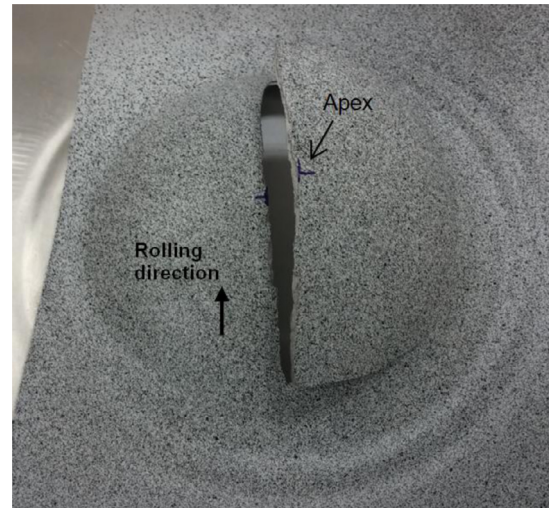


**Fig. 4.** Fractured specimen of AZ31B Mg sheet after bulge test with its position of apex.

rubber ring was inserted in the lower tool as shown in Fig. 3. Tests were conducted under the quasi-static condition at strain rates less than 0.002/s, and a holding force of 40,000 N was applied to the specimen.

The curvature and the in-plane strain distributions of the test specimen were measured by means of an optical device (Aramis) with special paint sprayed on the specimen. Specifically, the measured data within the radius of 16 mm around the apex of the deformed sheet were used to determine the curvature, while those within the radius of 5 mm were used for the determination of in-plane strains, by referring to the recommendation of range specified in ISO 16808:2014. An image of test specimen after bulge test was shown in Fig. 4 with its position of apex. It shows that the crack is formed along the rolling direction (which indicates the transverse direction of the sheet is the most vulnerable), and almost passes through the center of the bulged specimen with its nearest position less than 1 mm away from the apex.

By the condition of plastic incompressibility, strains through the thickness direction can be obtained from the measured in-plane strains. But here, it should be considered that during bulge tests, strain measurements are made in the middle of tests before unloading occurs. As a result, the measured strains contain components of elastic deformation. These elastic strains need to be subtracted from the measured strains before applying the condition of plastic incompressibility. In particular, the elastic deformation of AZ31B Mg sheet might be relatively large when compared to the plastic deformation in the range of small strains due to its

low elastic modulus. According to the generalized Hooke's law, the amount of elastic strain under the balanced biaxial loading condition is given by  $\sigma(1 - \nu)/E$  in each principal direction.

Test procedures and methods of measurement in this work are basically the same as those specified in ISO 16808:2014, but the calculations of thickness and stress were performed in a different manner considering the effect induced by the finite thickness of the sheet under bending deformation. This effect cannot be ignored to improve the accuracy of the calculated flow stress curves (Ranta-Eskola, 1979; Atkinson, 1997). Here, the biaxial flow stress curve was calculated following the procedure proposed by Vucetic et al. (2011). In their work, to minimize the effect of the finite thickness under bending deformation, the data measured on the upper surface of specimens were converted into the data based on the middle surface by using the following relationships:

$$\rho_m = \rho_s - \frac{t_m}{2}, e_{im} = e_{is} - \frac{t_m}{2\rho_m}, t_m = \frac{t_0}{(1 + e_{1m})(1 + e_{2m})},$$

$$\sigma = \frac{p\rho_m}{2t_m} \left(1 - \frac{t_m}{2\rho_m}\right)^2, \quad (25)$$

where  $\rho$ ,  $e_i$ ,  $t_0$ ,  $t$ ,  $p$  and  $\sigma$  denote the radius of curvature, the component of principal engineering strain, initial and current thicknesses of sheets, oil pressure and biaxial stress of the deformed sheet, respectively, while the subscript 's' denotes the data measured on the upper surface of the deformed sheet and the subscript 'm' denotes the data based on the middle surface of the deformed sheet. In Eq. (25), the values of  $\rho_s$ ,  $e_{is}$ ,  $t_0$  and  $p$  are provided by measurements.

The balanced biaxial flow stress curve obtained by following the above procedure was shown in Fig. 2(a). For small strains, the flow stress curve of the bulge test is generally not precise, since the test specimen initially has an almost infinite radius of curvature which makes it difficult to define the accurate stresses. But this initial inaccuracy of the flow stress curve disappears after subtracting elastic strains, since the very large radius of curvature of the specimen implies that the corresponding deformation is very small and within the elastic range. The initial yield stress of the balanced biaxial flow stress curve was determined in the same manner as the initial yield stress of the rolling direction at the same plastic work. The resulting initial balanced biaxial yield stress is listed in Table 1.

Comparing the flow stress curves shown in Fig. 2(a), it is obvious that the work hardening rate of the balanced biaxial flow stress curve is much higher than those of the flow stress curves measured along the rolling and transverse directions. To be more precise, each flow stress curve in Fig. 2(a) was shown again in Fig. 2(b) with its horizontal axis represented by the amount of plastic work per unit volume. This differential work hardening of AZ31B Mg sheet observed in Fig. 2(b) is also found in the work of Steglich et al. (2012), where it is observed that the contours of equal plastic work change their shape as deformation proceeds. The failure stress of the balanced biaxial flow stress curve and its plastic work equivalent stresses along the rolling and transverse directions were listed in Table 1. By comparing these values with the initial yield stresses, the relative change of the flow stress due to the differential work hardening can be estimated quantitatively.

### 3.3. Hemispherical dome test

The failure strains of AZ31B Mg sheet were measured by means of the hemispherical dome tests at room temperature with specimens of various widths to obtain failure strains depending on deformation paths. This procedure is similar to the conventional way of measuring the forming limit curve in the field of sheet metal forming, but the difference is in that the measured data are not the onset strains of the localized neck in the case of the Mg sheet.

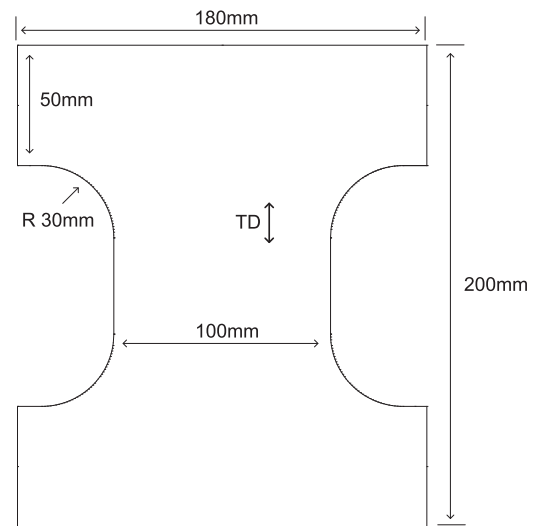


Fig. 5. An instance of the test specimen with its geometry and dimensions used in the hemispherical dome test.

The shape of the test specimen was carefully chosen with a slight modification of the design specified in the test standard ISO 12004-2:2008, taking into account the poor formability of AZ31B Mg sheet at room temperature. One instance of test specimens near the plane strain deformation mode is shown in Fig. 5 including its dimensions. Both end sections gripped by the holder have a rather larger width than the central section in order to reduce tensile stresses that might cause early failure at the section of grip. Mg sheet specimens can be easily broken especially at the position where the specimen meets the holder tool, since a relatively large bending deformation combined with a tensile force occurs at this position as the punch tool moves upward during tests.

Test specimens were prepared such that the transverse direction of the Mg sheet was aligned along the longer dimension of the specimen, as indicated in Fig. 5, to measure failure strains based on the transverse direction. The formability of AZ31B Mg sheet along the transverse direction is generally inferior to that of the other direction, which can be verified by tests such as the hydraulic bulge test and the hemispherical dome test whose loading paths are close to the balanced biaxial ones. In these tests, it is found that failure always occurs with cracks extended along the rolling direction (see Figs. 4 and 6(b)).

Circular grids whose diameter is 2.54 mm were marked on the surface of the specimen by a laser source to measure strains after deformation, as shown in Fig. 6. Lubricants were not used except for the test under the balanced biaxial loading condition in which Teflon sheets with a thickness of 0.1 mm were used. Without lubrication, friction force might delay failure by constraining the initiation or progress of localized deformation, but this effect of friction force is negligible in the case of AZ31B Mg sheet since its failure occurs mostly without localized deformation, which will be explained below. The punch tool has a diameter of 100 mm, while it moves with a speed of 60 mm/min during tests. Each test was stopped as soon as failure was observed in the specimen. Fractured specimens after hemispherical dome tests were shown in Fig. 6; one is close to the plane strain deformation, while the other is close to the balanced biaxial deformation.

The major and minor strains of each specimen were measured manually utilizing a portable video camera and its related analysis program. In strain measurements, 'fail' or 'safe' was judged in such a way that if a circular grid on the specimen was in contact with a fracture line, this grid was classified as 'fail', but if a circular grid closest to a fracture line was not in contact with the fracture line,

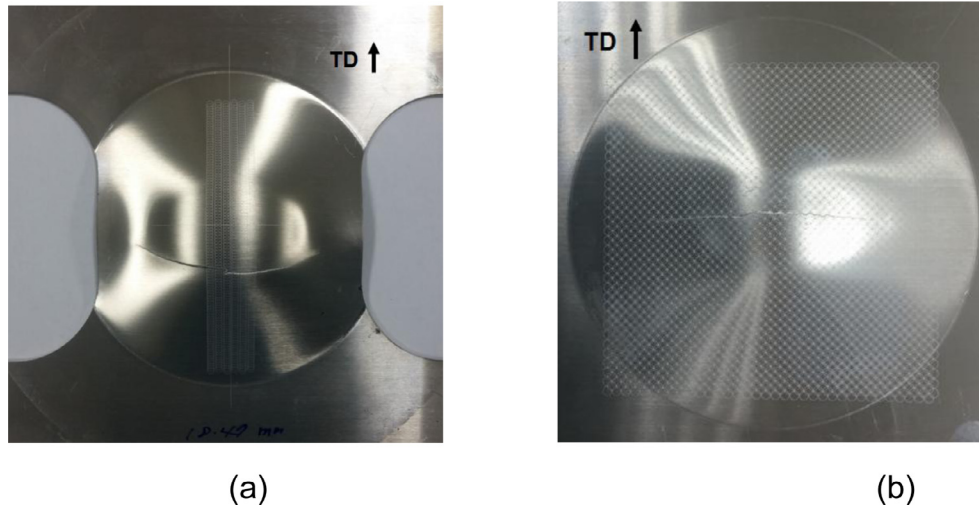


Fig. 6. Fractured specimens of AZ31B Mg sheet after hemispherical dome tests close to the (a) plane strain deformation and (b) balanced biaxial deformation.

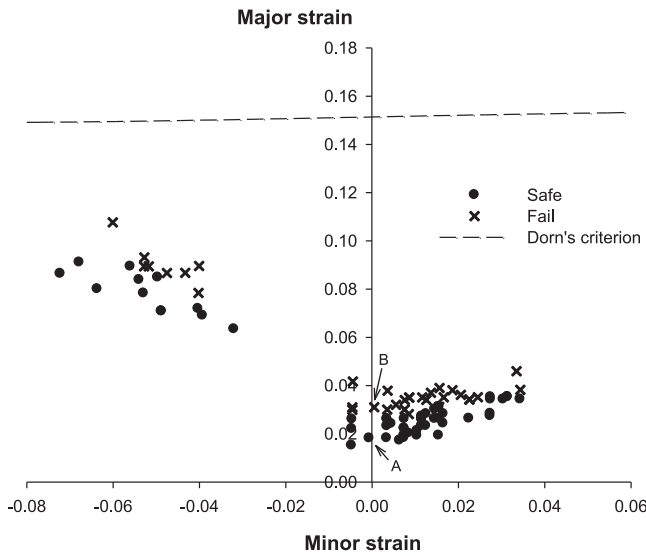


Fig. 7. 'Safe' and 'Fail' strains of the AZ31B Mg sheet measured by hemispherical dome tests shown in the principal strain space along with the prediction of Dorn's diffuse neck criterion.

then it was classified as 'safe'. Circular grids through which a fracture line passes were excluded from measurements. The measured strains of 'safe' and 'fail' were converted into the data based on the middle surface of the sheet in the same manner as the bulge test data were converted. The strains after conversion were shown in Fig. 7 in the principal strain space. Taking a close look at the strain data in Fig. 7, it is observed that the boundary that divides the strains of 'fail' and 'safe' is not clear, i.e., strains classified as 'fail' are found in the area of 'safe' strains and vice versa. This can be attributed to the deviation of material properties of the Mg sheet specimens measured.

Dorn and Thomsen (1947) proposed the onset condition of diffuse neck that the diffuse neck forms as one of biaxial loading reaches the maximum value. Chung et al. (2011) derived the generalized form of Dorn's criterion under the proportional loading condition with the Swift hardening equation, and it is defined as

$$(\varepsilon_2^p)_d = n - \frac{\bar{\varepsilon}_0^p}{G(\beta)}, (\varepsilon_1^p)_d = \frac{K_0\beta - 1}{K_{90} - \beta} (\varepsilon_2^p)_d, \quad (26)$$

where  $n$  is the work hardening exponent, while  $(\varepsilon_1^p)_d$  and  $(\varepsilon_2^p)_d$  are the onset strains of diffuse neck along each principal direction. Using the material coefficients listed in Table 2 along with Eq. (26), the onset condition of diffuse neck of AZ31B Mg sheet was calculated and shown in Fig. 7, where it is observed that the calculated line of diffuse neck is located far above the 'safe' and 'fail' strains of AZ31B Mg sheet. This result theoretically proves the fact that the failure of AZ31B Mg sheet occurs mostly without diffuse neck. In certain deformation modes, however, such as the simple tension and its neighboring deformation modes, the diffuse neck does occur as indicated by the simple tension curves shown in Fig. 2(a). Nonetheless, it is now certain that the failure of AZ31B Mg sheet at room temperature is unable to be well predicted by the localized necking model whose onset condition is more severe than that of diffuse neck.

### 3.4. Determination of material coefficients

The failure prediction equation in Eq. (18) has a total of 9 material coefficients to be determined. Among these coefficients,  $K$ ,  $\bar{\varepsilon}_0^p$  and  $n$  were already determined by fitting the hardening curve with the Swift equation in Eq. (14). It is very straightforward to obtain  $K_0$  and  $K_{90}$  as well as the coefficient of the normal anisotropy  $\bar{K}$  in Eq. (19) from the measured  $R$ -values listed in Table 1 by using the relationship given in Eqs. (9) and (20). The critical shear stress  $k_{TD}$  was determined by referring to the failure stress of the bulge test (whose magnitude is equal to 350.8 MPa) with Eq. (15). Determining  $k_{TD}$  from the failure stress of the bulge test can be considered reasonable by observing that the fractured specimen of the bulge test in Fig. 4 shows failure in the transverse direction. On the other hand, the failure stress of simple tension test is not appropriate to be used as a reference value for the critical shear stress, since the failure of simple tension test occurs after diffuse neck forms as mentioned earlier, and this makes it difficult to characterize the true failure stress.

It is not so straightforward, however, to determine the coefficients of the yield function (i.e.,  $X$ ,  $Y$  and  $B$  in Eq. (4)) due to the differential work hardening behavior of AZ31B Mg sheet as shown in Fig. 2. The relative yield stress ratio between each hardening curve varies as the amount of plastic work increases and this variation is more prominent in the flow curve of the balanced biaxial loading condition. For this reason, the material coefficients to represent the yield stresses of AZ31B Mg sheet should be determined carefully. Considering the differential work hardening of AZ31B Mg

sheet, two sets of material coefficients for the yield function were obtained here, i.e.,  $(X, Y, B)$  and  $(X', Y', B')$ , where  $X, Y$  and  $B$  are more related to the size of the yield function defining the failure stress, while  $X', Y'$  and  $B'$  are more related to the amount of total plastic strain at failure reflecting the shape change of the yield function during integration of plastic strain rate. The procedures to obtain these coefficients will be explained below. To begin with, the amount of total plastic work up to failure under the plane strain deformation condition (which will be denoted by  $W_f^{PS}$ ) needs to be calculated.

### 3.4.1. Calculations of $W_f^{PS}$

By definition, the total plastic work up to failure under the plane strain deformation condition can be represented by the equation  $W_f^{PS} = \int_0^{\varepsilon_f^{PS}} \sigma^P d\varepsilon^P$ , where  $\sigma^P$  and  $\varepsilon_f^{PS}$  denote the stress and failure plastic strain under the plane strain deformation condition. To obtain the magnitude of  $W_f^{PS}$ , the flow curve measured under plane strain deformation is needed, but it is not readily measurable. Therefore, the magnitude of  $W_f^{PS}$  was obtained indirectly by utilizing the strains measured from the hemispherical dome tests as well as the uniaxial hardening curve measured along the transverse direction. As indicated in Fig. 7, the two points A and B which lie close to the plane strain deformation path were selected, and these points are the 'safe' and 'fail' strains, respectively. Provided that failure under plane strain deformation occurs at the average value of major strains of these two points, the failure strain under the plane strain deformation path is obtained by

$$\varepsilon_f^{PS} = \frac{\varepsilon_M^A + \varepsilon_M^B}{2}, \quad (27)$$

where  $\varepsilon_M^A$  and  $\varepsilon_M^B$  denote the major strains of points A and B, respectively. The plastic work equivalence principle with the assumption of proportional loading leads to the following relationship:

$$\bar{\sigma} \bar{\varepsilon}^P = \sigma_i \varepsilon_i^P = \sigma_2^{ST} \varepsilon_2^{ST} = \sigma_1^{PS} \varepsilon_1^{PS} + \sigma_2^{PS} \varepsilon_2^{PS} = \sigma_2^{PS} \varepsilon_2^{PS}, \quad (28)$$

where the superscripts 'ST' and 'PS' denote the simple tension and plane strain deformation modes, respectively, while the direction 2 is chosen to be the major direction of deformation, so that the minor strain  $\varepsilon_1^{PS}$  becomes zero under the plane strain deformation condition. From Eq. (28), it follows that

$$\sigma_2^{PS} = \gamma \sigma_2^{ST}, \quad \varepsilon_2^{PS} = \frac{1}{\gamma} \varepsilon_2^{ST}, \quad (29)$$

where  $\gamma$  denotes a proportionality constant of the magnitude of stress (or strain) between two different deformation modes (i.e., ST and PS). Within the framework of the maximum shear stress criterion, it is supposed that the Mg sheet fails as its major stress reaches the failure stress  $\sigma_f$  given in Eq. (15). Therefore, under the plane strain deformation condition, failure occurs at the condition  $\sigma_2^{PS} = \sigma_f$ , and the corresponding plastic strain (i.e.,  $\varepsilon_2^{PS}$ ) at this failure point is simply the failure strain  $\varepsilon_f^{PS}$  defined in Eq. (27). Accordingly, the proportionality constant  $\gamma$  can be obtained using the following condition:

$$\gamma = \frac{\sigma_f}{\sigma_2^{ST}} = \frac{\varepsilon_2^{ST}}{\varepsilon_f^{PS}}. \quad (30)$$

Here,  $\sigma_2^{ST}$  and  $\varepsilon_2^{ST}$  are dependent quantities whose relationship is found by the simple tension test along the transverse direction. To find the value of the proportionality constant  $\gamma$ , both of the stress ratio  $\sigma_f/\sigma_2^{ST}$  and the plastic strain ratio  $\varepsilon_2^{ST}/\varepsilon_f^{PS}$  in Eq. (30) were plotted as a function of plastic strain in Fig. 8, where the intersection point P of these two curves determines the

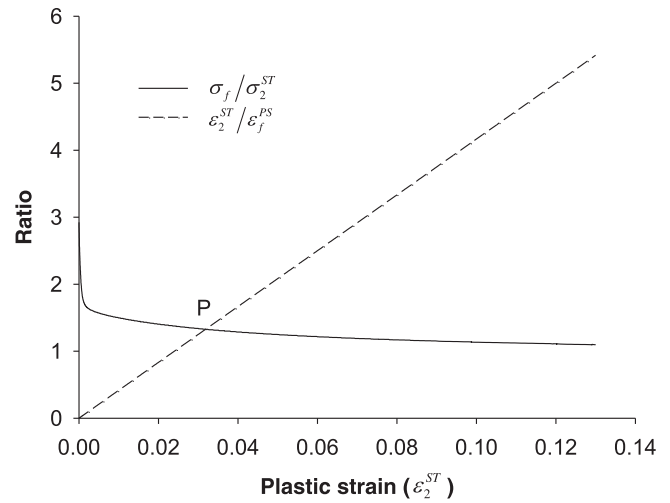


Fig. 8. Graphical representation of the stress ratio  $\sigma_f/\sigma_2^{ST}$  and the plastic strain ratio  $\varepsilon_2^{ST}/\varepsilon_f^{PS}$  to determine the proportionality constant  $\gamma$ .

Table 3

Magnitudes of the mechanical quantities used to determine the coefficients of yield function.

$\gamma$	$\sigma_2^{STa}$ (MPa)	$\varepsilon_f^{PS}$	$\varepsilon_2^{STa}$	$W_f^{PS}$ (mJ/mm <sup>3</sup> )	$\varepsilon_f^b$	$\varepsilon_{W_f^{PS}}^b$	$\varepsilon_B^b$
1.33	264.3	0.024	0.032	7.69	0.052	0.030	0.038

<sup>a</sup> The value of this quantity is the one to satisfy Eq. (30).

magnitude of the proportionality constant  $\gamma$  along with the corresponding values of  $\sigma_2^{ST}$  and  $\varepsilon_2^{ST}$ . Once  $\gamma$  is determined, the plastic work equivalent stresses and plastic strains between simple tension and plane strain deformation modes can be found from Eq. (29) at any point of stress (or strain). The magnitude of  $W_f^{PS}$  can then be obtained by integrating the uniaxial hardening curve of the transverse direction up to the plastic strain determined by Eq. (30), i.e.,

$$W_f^{PS} = \int_0^{\gamma \varepsilon_f^{PS}} \sigma_2^{ST} d\varepsilon_2^P. \quad (31)$$

The magnitudes of the mechanical quantities contained in Eqs. (30) and (31) are summarized in Table 3.

### 3.4.2. Coefficients X, Y and B

In failure predictions of materials having differential work hardening, the yield stresses around the small deformation range are not closely related to material failure since failure usually occurs at large strains. Therefore, the coefficient  $B$  was determined by taking the mean value of balanced biaxial stresses for the specific interval close to the failure point, i.e.,

$$B = \frac{\int_{\varepsilon_{W_f^{PS}}^b}^{\varepsilon_f^b} \sigma^b d\varepsilon^P}{\varepsilon_f^b - \varepsilon_{W_f^{PS}}^b}, \quad (32)$$

where  $\sigma^b$  and  $\varepsilon_f^b$  denote the stress and the failure plastic strain of the balanced biaxial flow curve, while  $\varepsilon_{W_f^{PS}}^b$  denotes the specific plastic strain of the balanced biaxial flow curve at which the total plastic work per unit volume (i.e.,  $\int_0^{\varepsilon_f^b} \sigma^b d\varepsilon^P$ ) is equal to the magnitude of  $W_f^{PS}$  obtained in the previous section (see Fig. 9 for its definition).

In biaxial deformation modes, the total plastic work up to failure (denoted by  $W_f$ ) generally has its minimum when the defor-



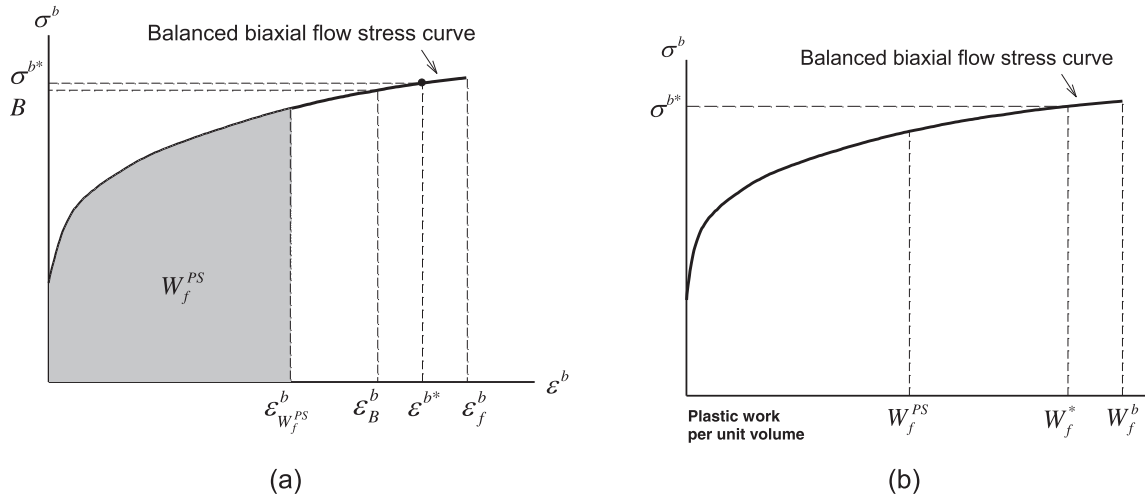


**Fig. 9.** Schematic illustration of (a) the definition of plastic strains  $\epsilon_{W_f^{PS}}^b$ ,  $\epsilon_B^b$  and  $\epsilon_f^b$  and (b) the relationship between quantities of plastic work per unit volume  $W_f^{PS}$ ,  $W_f^*$  and  $W_f^b$ .

mation mode is close to the plane strain mode, whereas  $W_f$  has its maximum when the deformation is close to the balanced biaxial deformation mode. Accordingly, the amount of  $W_f$  of any other biaxial deformation mode has a value somewhere between those of plane strain and balanced biaxial deformations. For instance, suppose that the Mg sheet deforms along a certain deformation path  $\delta^*$  ( $= (d\epsilon_1^p/d\epsilon_2^p)^*$ ) which lies between the plane strain and the balanced biaxial deformation modes (i.e.,  $0 < \delta^* < 1$ ), then  $W_f$  of the deformation path  $\delta^*$  lies in a condition that  $W_f^{PS} < W_f^* < W_f^b$ , where  $W_f^b$  denotes  $W_f$  of the balanced biaxial loading path. From the plastic work equivalence principle, a point corresponding to the magnitude of  $W_f^*$  can be found in the balanced biaxial flow stress curve, along with its associated stress  $\sigma^{b*}$  and plastic strain  $\epsilon^{b*}$ , as shown in Fig. 9(a) and (b). Consequently, the coefficient  $B$  defined in Eq. (32) is equivalent to the mean value of the stress  $\sigma^{b*}$  for the interval from  $W_f^{PS}$  to  $W_f^b$  considering  $W_f$  of all the biaxial deformations from plane strain to balanced biaxial modes. The deformation path of negative minor strain (i.e.,  $\delta < 0$ ) and its  $W_f$  were not considered here to determine the coefficient  $B$ , since they are not much related to the magnitude of the coefficient  $B$ .

The magnitudes of plastic strains  $\epsilon_f^b$  and  $\epsilon_{W_f^{PS}}^b$  to calculate the coefficient  $B$  in Eq. (32) were listed in Table 3. After the coefficient  $B$  was determined, the coefficients  $X$  and  $Y$  were determined by finding the yield stresses along the rolling and transverse directions at the plastic work equal to that of the balanced biaxial yield stress  $B$ .

### 3.4.3. Coefficients $X'$ , $Y'$ and $B'$

In Eqs. (12) and (13), the coefficients of yield function (i.e.,  $X$ ,  $Y$  and  $B$ ) are also found in the function  $G(\beta)$ . Note that Eq. (12) was obtained by integrating Eq. (11) from the initial to the current states assuming the material coefficients of the function  $G(\beta)$  are constant. However, in the case of materials exhibiting differential work hardening, such as the AZ31B Mg sheet, the relative magnitudes between the coefficients  $X$ ,  $Y$  and  $B$  cannot be regarded as constant during integration. Therefore, Eq. (12) is not an accurate representation of integration of Eq. (11) under such conditions. To resolve this and simplify calculations, it was assumed that the hardening dependent coefficients  $X$ ,  $Y$  and  $B$  were approximately represented by some average scalar values during integration of the plastic strain rate. Let these new average coefficients be denoted by  $X'$ ,  $Y'$  and  $B'$ , and with these coefficients, the function

$G(\beta)$  was redefined by

$$G'(\beta) = \frac{K_0\beta^2 - 2\beta + K_{90}}{\sqrt{\frac{Y'^2}{X'^2}\beta^2 - \left(1 + \frac{Y'^2}{X'^2} - \frac{Y'^2}{B'^2}\right)\beta + 1}} \quad (K_{90} - \beta) \quad (33)$$

By definition, the coefficients  $X'$ ,  $Y'$  and  $B'$  in the function  $G'(\beta)$  represent the average shape of the yield function taking into account the change from the initial state to the current state, while the shape of yield function at the moment of failure is defined by the coefficients  $X$ ,  $Y$  and  $B$  obtained in the previous section. With this in mind, the coefficient  $B'$  in Eq. (33) was obtained by taking the mean value of balanced biaxial stresses for the interval from the initial yield to the current stress  $B$  as follows:

$$B' = \frac{\int_0^{\epsilon_B^b} \sigma^b d\epsilon^p}{\epsilon_B^b}, \quad (34)$$

where  $\epsilon_B^b$  denotes the corresponding plastic strain of the stress  $B$  in the balanced biaxial flow stress curve (see Fig. 9(a)). The magnitude of  $\epsilon_B^b$  is listed in Table 3. The associated coefficients  $X'$  and  $Y'$  were determined by finding the yield stresses along the rolling and transverse directions at the plastic work equal to that of the balanced biaxial yield stress  $B'$ .

The material coefficients obtained above are summarized in Table 2. In Fig. 10, the yield loci of the normalized yield functions with coefficients of both  $(X, Y, B)$  and  $(X', Y', B')$  were presented along with the locus of the normalized plastic potential  $\Phi$  in the first quadrant of normalized principal stress space. The yield locus of the isotropic yield function was also shown in Fig. 10 for comparison purposes, and it reveals the higher yield stresses of the other yield functions around the balanced biaxial loading path. Especially, the yield function used in the AFR shows the highest balanced biaxial yield stress. The locus of the normalized yield function whose coefficients obtained from the initial yield stresses listed in Table 1 was also shown in Fig. 10, and comparing it with the other yield loci shows the transition of the yield function with plastic deformation.

## 4. Result and discussion

The analytical expressions for the failure prediction of AZ31B Mg sheet at room temperature developed in the previous section (i.e., Eqs. (18), (19), (23) and (24)) are summarized in Table 4 along

**Table 4**  
Equations of failure prediction with the conditions for their derivation.

Minor failure strain $(\varepsilon_1^p)_f$	Major failure strain $(\varepsilon_2^p)_f$	No.	Conditions
$\frac{K_0\beta - 1}{K_{90} - \beta} (\varepsilon_2^p)_f$	$\frac{\left(\frac{Y^2}{X^2}\beta^2 - \left(1 + \frac{Y^2}{X^2} - \frac{Y^2}{B^2}\right)\beta + 1\right) \frac{1}{2n} \left(\frac{2k_{TD}}{K}\right)^{\frac{1}{n}} - \bar{\varepsilon}_0^p}{G(\beta)}$	Eq. (18)	NAFR, planar anisotropy
$\frac{\bar{K}\beta - 1}{\bar{K} - \beta} (\varepsilon_2^p)_f$	$\frac{\left(\beta^2 - \left(2 - \frac{Y^2}{B^2}\right)\beta + 1\right) \frac{1}{2n} \left(\frac{2k_{TD}}{K}\right)^{\frac{1}{n}} - \bar{\varepsilon}_0^p}{\bar{G}(\beta)}$	Eq. (19)	NAFR, normal anisotropy
$\frac{K_0\beta - 1}{K_{90} - \beta} (\varepsilon_2^p)_f$	$\frac{\left(\frac{K_0}{K_{90}}\beta^2 - \frac{2\beta}{K_{90}} + 1\right) \frac{1}{2n} \left(\frac{2k_{TD}}{K}\right)^{\frac{1}{n}} - \bar{\varepsilon}_0^p}{\sqrt{K_{90}}\sqrt{K_0\beta^2 - 2\beta + K_{90}}} (K_{90} - \beta)$	Eq. (23)	AFR, planar anisotropy
$\frac{2\beta - 1}{2 - \beta} (\varepsilon_2^p)_f$	$\frac{(\beta^2 - \beta + 1) \frac{1}{2n} \left(\frac{2k}{K}\right)^{\frac{1}{n}} - \bar{\varepsilon}_0^p}{2\sqrt{\beta^2 - \beta + 1}} (2 - \beta)$	Eq. (24)	Isotropy

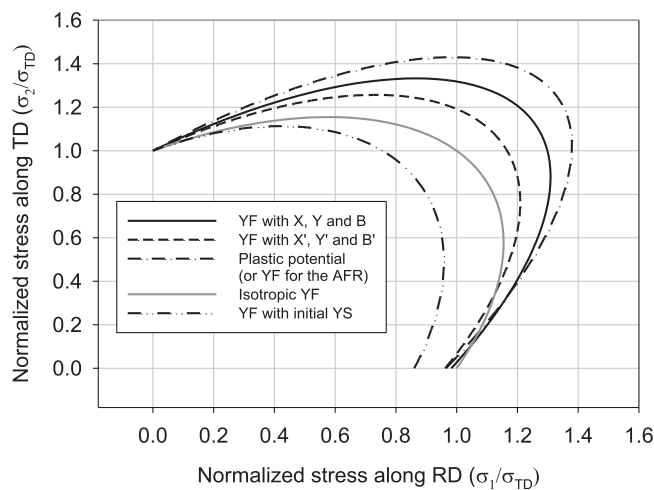


**Fig. 10.** Loci of the yield function (YF) with different sets of anisotropy coefficients as well as the plastic potential (or yield function used with the AFR) shown in the normalized principal stress space.

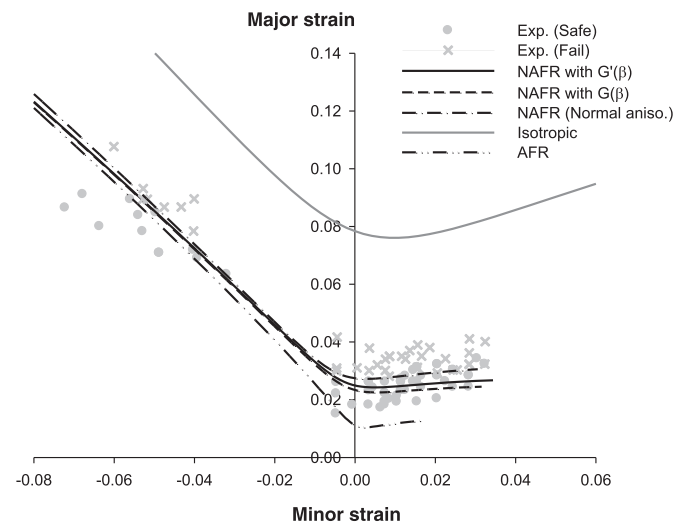


**Fig. 11.** Comparison of failure prediction curves obtained from equations in Table 4 with the experimental data of failure strains measured by the hemispherical dome test.

with the condition for each equation. These equations are functions of the stress ratio  $\beta$  whose range varies from 0 to 1, while the principal direction 2 (or the transverse direction) was chosen to be the major direction of deformation. The failure predictions using these equations can be validated by comparing them with the experimental failure strains measured by the hemispherical dome test. With the material coefficients listed in Table 2, equations in Table 4 were evaluated and the resulting curves are shown in the principal strain space along with the experimental data of strain measurements in Fig. 11. As a whole, the failure prediction equation based on the NAFR shows a better accuracy than the other equations based on the isotropic condition or the AFR.

It can be seen that the failure prediction made by the equation of isotropic assumption is far above the experimentally measured 'fail' strains of the AZ31B Mg sheet, giving a poor failure prediction. It is obvious that this discrepancy resulted from ignoring the strong anisotropic properties of AZ31B Mg sheet such as the large  $R$ -values and different yield stresses for different loading paths. This implies that in dealing with materials of strong anisotropy, such as AZ31B Mg sheets, their anisotropic properties should not be ignored to make a good failure prediction. In Fig. 11, it is also found that the failure prediction made by the equation based on the AFR is not precise, giving a low estimation of failure strain. This result primarily came from the limited number of co-

efficients of anisotropy in the formulation (see Eq. (23)) by using the AFR with the quadratic anisotropic yield function. In addition to this, there is another reason that the quadratic yield function whose coefficients of anisotropy are obtained from the measured  $R$ -values tends to give a highly overestimated value of balanced biaxial yield stress as the  $R$ -value is very large. In the normalized principal stress space in Fig. 10, the locus of the plastic potential or the yield function of the AFR (both are in effect the same functions in that they take  $R$ -values for their coefficients of anisotropy) shows a normalized balanced biaxial yield stress higher than that of any other yield locus in Fig. 10. It is even higher than the normalized failure stress measured by the bulge tests. For example, a quantitative evaluation of the yield function in Eq. (22) with the  $R$ -values listed in Table 2 gives a balanced biaxial yield stress of 373.3 MPa as the yield stress along the transverse direction has a magnitude of 287.4 MPa. However, at the same yield stress along the transverse direction, the experimental measurement gives a balanced biaxial yield stress of 350.8 MPa (see Table 1) by the plastic work equivalence. Such an overestimated balanced biaxial yield stress produced by the yield function of the AFR leads to inaccuracy of failure prediction especially in the biaxial deformation area.

In Fig. 11, it can be seen that the failure predictions made by the equations based on the NAFR are close to the boundary be-

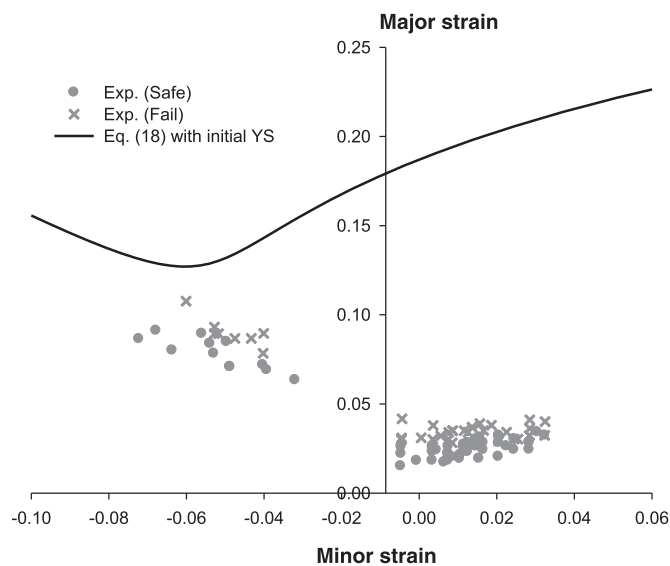


**Fig. 12.** Failure prediction without considering the differential work hardening of AZ31B Mg sheet by employing Eq. (18) with the initial yield stresses assigned to the material coefficients  $X$ ,  $Y$  and  $B$ .

tween the experimental 'safe' and 'fail' strains of AZ31B Mg sheet, although they are not perfectly in agreement with that boundary. There are three kinds of failure prediction curves based on the NAFR in Fig. 11; two of them are obtained from Eq. (18) under the planar anisotropy condition, while the other curve is obtained from Eq. (19) under the normal anisotropy condition. In order to take into account the differential work hardening behavior of AZ31B Mg sheet, one of the failure prediction curves based on Eq. (18) was obtained by using the function  $G'(\beta)$  in Eq. (28) instead of using the function  $G(\beta)$  in Eq. (13) (or Eq. (18)). As can be seen from Fig. 11, the failure prediction curve taking into account the differential work hardening during integration of the plastic strain rate (i.e., NAFR with  $G'(\beta)$  in Fig. 11) shows a slightly better accuracy than the other curve obtained with  $G(\beta)$ . Meanwhile, by imposing the condition of normal anisotropy, the failure prediction curve slightly shifts upwards showing a better agreement with experimental data. However, this does not mean that Eq. (19), an equation of normal anisotropy, has better accuracy than Eq. (18), an equation of more general anisotropy. Rather, it would be more reasonable to understand this in such a way that the failure prediction with Eq. (19) is within the error bound of the failure prediction with Eq. (18). The difference made by the assumption of normal anisotropy is not so significant. Note that in the evaluation of Eq. (19), the material coefficients  $Y'$  and  $B'$  in Table 2 were used for the function  $\bar{G}(\beta)$ , instead of  $Y$  and  $B$ , to consider the differential work hardening.

In order to assess the influence made by entirely ignoring the differential work hardening, a failure prediction was made by using the initial yield stresses listed in Table 2, as is always done under the condition of isotropic hardening. Initial yield stresses were assigned to the material coefficients  $X$ ,  $Y$  and  $B$  of the yield function and the function  $G(\beta)$ . For the failure prediction, Eq. (18) was employed. The values of the other material coefficients are the same as those listed in Table 2, while the conditions of  $X=X'$ ,  $Y=Y'$  and  $B=B'$  are valid here. The result is shown in Fig. 12 with axis scales different to those in Fig. 11. It is shown that there is a large discrepancy between the failure prediction curve and the experimental failure strains. This result verifies the importance of considering the differential work hardening in the failure predictions of AZ31B Mg sheet.

For the failure prediction equations in Table 4, the major strain of failure under the plane strain deformation condition can be easily obtained, for example, by substituting the condition  $\beta = 1/K_0$  into Eq. (18). However, the minimum point of the failure prediction curve does not lie in the plane strain deformation path, as shown in Fig. 11. As for the equations in Table 4, it is not easy to obtain the analytical expression for the minimum value of major failure strain, even for the simplest equation such as the isotropic one, so that numerical approaches are required to find the minimum.

## 5. Conclusion

To make failure predictions of AZ31B Mg sheets, analytical expressions were derived in this work based on the maximum shear stress criterion in conjunction with the quadratic anisotropic yield function and the plastic potential. Equations of failure prediction with different levels of material anisotropy were derived by adopting different flow rules (AFR and NAFR) as well as by imposing restrictions on the coefficients of anisotropy. Failure predictions were made and compared with the experimentally measured failure strains. It was found that failure predictions made by using the equation of NAFR gave the best accuracy, and the further assumption of normal anisotropy with this equation also gave a reasonable accuracy. However, the failure prediction with an assumption of material isotropy made an inaccurate prediction showing large differences from the experimentally measured failure strains. Failure prediction with the equation of AFR also showed a deviation from the experimental failure strains, which results from the limited number of coefficients of anisotropy in the equation as well as the overestimated balanced biaxial yield stress made by the large  $R$ -values of AZ31B Mg sheet in using the quadratic anisotropic yield function.

The procedure to determine the coefficients of anisotropy considering the differential work hardening of AZ31B Mg sheet was addressed. It was found that the consideration of differential work hardening to obtain material coefficients gave better accuracy in failure prediction, and ignoring the differential work hardening by using the initial yield stresses led to a totally wrong failure prediction.

The validity of the maximum shear stress criterion for the failure prediction of AZ31B Mg sheet under stretching deformation conditions was verified by the results of this work. However, it was also found that without proper considerations on anisotropy and differential work hardening, the failure of AZ31B Mg sheet cannot be well predicted despite the use of the maximum shear stress criterion. This implies that in failure predictions of materials exhibiting strong anisotropy and/or differential work hardening, anisotropy and hardening characteristics should be treated with the same level of importance with a failure criterion itself.

## Acknowledgments

This work was financially supported by the Mg Material R&D Project for the Super-light Vehicle operating for the execution of WPM (World Premier Materials) Program funded by the Ministry of Trade, Industry and Energy, Republic of Korea. The authors would like to thank Dr. David Klaumünzer (Volkswagen AG) for his assistance and helpful comments.

## References

- Agnew, S.R., Duygulu, Ö., 2005. Plastic anisotropy and the role of non-basal slip in magnesium alloy AZ31B. *Int. J. Plast.* 21, 1161–1193.
- Atkinson, M., 1997. Accurate determination of biaxial stress-strain relationships from hydraulic bulging tests of sheet metals. *Int. J. Mech. Sci.* 39, 761–769.
- Bohlen, J., Nürnberg, M.R., Senn, J.W., Letzig, D., Agnew, S.R., 2007. The texture and anisotropy of magnesium–zinc–rare earth alloy sheets. *Acta Mater.* 55, 2101–2112.

- Chung, K., Ahn, K., Yoo, D.H., Chung, K.H., Seo, M.H., 2011. Formability of TWIP (twinning induced plasticity) automotive sheets. *Int. J. Plast.* 27, 52–81.
- Cubberly, W.H., Baker, H., Benjamin, D., Unterweiser, P.M., Kirkpatrick, C.W., Knoll, V., Nieman, K. (Eds.), 1979. *Properties and Selection: Nonferrous Alloys and Pure Metals* (Metals Handbook), ninth ed. American Society for Metals.
- Doege, E., Droder, K., 2001. Sheet metal forming of magnesium wrought alloys—formability and process technology. *J. Mater. Process. Technol.* 115, 14–19.
- Dorn, J.E., Thomsen, E.G., 1947. The ductility of metals under general conditions of stress and strain. *Trans. Am. Soc. Met.* 39, 741–772.
- Hill, R., 1948. A theory of the yielding and plastic flow of anisotropic metals. *Proc. R. Soc. A* 193, 281–297.
- Hill, R., 1952. On discontinuous plastic states with special reference to localized necking in thin sheets. *J. Mech. Phys. Solids* 1, 19–30.
- Huang, X., Suzuki, K., Saito, N., 2009. Textures and stretch formability of Mg–6Al–1Zn magnesium alloy sheets rolled at high temperatures up to 793 K. *Scr. Mater.* 60, 651–654.
- Kim, J., Ryou, H., Kim, D., Kim, D., Lee, W., Hong, S., Chung, K., 2008. Constitutive law for AZ31B Mg alloy sheets and finite element simulation for three point bending. *Int. J. Mech. Sci.* 50, 1510–1518.
- Li, Y., Luo, M., Gerlach, J., Wierzbicki, T., 2010. Prediction of shear-induced fracture in sheet metal forming. *J. Mater. Process. Technol.* 210, 1858–1869.
- Lin, J., Chan, L.C., Wang, L., 2010. Prediction of forming limit diagrams based on shear failure criterion. *Int. J. Solids Struct.* 47, 2855–2865.
- Lou, X.Y., Li, M., Boger, R.K., Agnew, S.R., Wagoner, R.H., 2007. Hardening evolution of AZ31B Mg sheet. *Int. J. Plast.* 23, 44–86.
- Marciniak, Z., Kuczynski, K., 1967. Limits strains in the processes of stretch-forming sheet metal. *Int. J. Mech. Sci.* 9, 609–612.
- Neil, C.J., Agnew, S.R., 2009. Crystal plasticity-based forming limit prediction for non-cubic metals: application to Mg alloy AZ31B. *Int. J. Plasticity* 25, 379–398.
- Park, T., Chung, K., 2012. Non-associated Flow rule with symmetric stiffness modulus for isotropic-kinematic hardening. *Int. J. Solids Struct.* 49, 3582–3593.
- Ranta-Eskola, A.J., 1979. Use of the hydraulic bulge test in biaxial tensile testing. *Int. J. Mech. Sci.* 21, 457–465.
- Shackelford, J.F., 2009. *Introduction to Materials Science for Engineers*, eighth ed. Pearson.
- Steglich, D., Jeong, Y., Andar, M.O., Kuwabara, T., 2012. Biaxial deformation behaviour of AZ31 magnesium alloy: crystal-plasticity-based prediction and experimental validation. *Int. J. Solids Struct.* 49, 3551–3561.
- Stoughton, T.B., 2002. A non-associated flow rule for sheet metal forming. *Int. J. Plast.* 18, 687–714.
- Suh, B.C., Shim, M.S., Shin, K.S., Kim, N.J., 2014. Current issues in magnesium sheet alloys: where do we go from here? *Scr. Mater.* 84–85, 1–6.
- Vucetic, M., Bouguecha, A., Peshekhodov, I., Götze, T., Huinink, T., Friebe, H., Möller, T., Behrens, B.A., 2011. Numerical validation of analytical biaxial true stress-true strain curves from the bulge test. *AIP Conf. Proc.* 1383, 107–114.
- Wang, H., Wu, P.D., Boyle, K.P., Neale, K.W., 2011. On crystal plasticity formability analysis for magnesium alloy sheets. *Int. J. Solids Struct.* 48, 1000–1010.
- Wang, H., Wu, P.D., Lee, S.Y., Wang, J., Neale, K.W., 2015. Numerical study of the effects of shear deformation and superimposed hydrostatic pressure on the formability of AZ31B sheet at room temperature. *Int. J. Mech. Sci.* 92, 70–79.
- Wierzbicki, T., Bao, Y., Lee, Y.W., Bai, Y., 2005. Calibration and evaluation of seven fracture models. *Int. J. Mech. Sci.* 47, 719–743.